Chemistry–A European Journal
Research Article
doi.org/10.1002/chem.202104121
Chemistry Europe
European Chemical Societies Publishing
www.chemeurj.org

Inverse-Tunable Red Luminescence and Electronic Properties of Nitridoberylloaluminates $Sr_{2-x}Ba_x[BeAl_3N_5]:Eu^{2+}$ ($x = 0$–2)

Eugenia Elzer,[a] Philipp Strobel,[b] Volker Weiler,[b] Muhammad R. Amin,[c] Peter J. Schmidt,[b] Alexander Moewes,[c] and Wolfgang Schnick*[a]

Abstract: The nitridoberylloaluminate $Ba_2[BeAl_3N_5]:Eu^{2+}$ and solid solutions $Sr_{2-x}Ba_x[BeAl_3N_5]:Eu^{2+}$ ($x = 0.5$, 1.0, 1.5) were synthesized in a hot isostatic press (HIP) under 50 MPa N_2 atmosphere at 1200 °C. $Ba_2[BeAl_3N_5]:Eu^{2+}$ crystallizes in triclinic space group $P\bar{1}$ (no. 2) ($Z = 2$, $a = 6.1869(10)$, $b = 7.1736(13)$, $c = 8.0391(14)$ Å, $\alpha = 102.754(8)$, $\beta = 112.032(6)$, $\gamma = 104.765(7)$°), which was determined from single-crystal X-ray diffraction data. The lattice parameters of the solid solution series have been obtained from Rietveld refinements and show a nearly linear dependence on the atomic ratio Sr:Ba. The electronic properties and the band gaps of $M_2[BeAl_3N_5]$ (M = Sr, Ba) have been investigated by a combination of soft X-ray spectroscopy and density functional theory (DFT) calculations. Upon irradiation with blue light (440–450 nm), the nitridoberylloaluminates exhibit intense orange to red luminescence, which can be tuned between 610 and 656 nm (fwhm = 1922–2025 cm^{-1} (72–87 nm)). In contrast to the usual trend, the substitution of the smaller Sr^{2+} by larger Ba^{2+} leads to an inverse-tunable luminescence to higher wavelengths. Low-temperature luminescence measurements have been performed to exclude anomalous emission.

Introduction

In recent years, the constant search for new phosphors pushed solid-state lighting, based on light-emitting diodes (LEDs), to one of the most popular lighting solutions. Especially, further improving luminous efficacy of white phosphor-converted (pc) LEDs with high color rendition depends on phosphor materials with optimized luminescence properties.[1] The combination of a high color rendering index without compromising luminous efficacy is a key factor in the optimization of pc-LEDs.[2] Here, particularly the emission maximum and the width of the emission band of the red-emitting phosphor play a significant role to avoid emission in the deep red spectral area.

In this context, Eu^{2+} doped nitrides are intensively investigated, as they do not only show good thermal and chemical stability, but also promising optical properties.[3] The luminescence observed in Eu^{2+} activated phosphors can be generally attributed to transitions between the $4f^6(^7F)5d^1$ exited state and the $4f^7(^8S_{7/2})$ ground state and is highly sensitive towards the local environment of the activator ion.[4] Red-emitting nitrides like $(Sr,Ba)_2Si_5N_8:Eu^{2+}$[5] or $(Ca,Sr)AlSiN_3:Eu^{2+}$[6] already found their way into commercial application as phosphors in pc-LEDs, due to their excellent photoluminescence properties. However, since both compounds exhibit rather broad emission bands, the luminous efficacy is limited due to spill-over to the infrared region. Structures based on highly condensed anionic networks are shown to be beneficial for narrow-band emission.

The degree of condensation κ is defined as the ratio of tetrahedral centers T to coordinating N atoms ($\kappa = n(T):n(N)$). In theory κ can be increased by replacing higher charged tetrahedral centers (Al^{3+}, Si^{4+}) with lower charged ones like Li^+ or Mg^{2+}. Indeed, these substitutions led to the discovery of promising narrow-band red-emitting phosphors, such as $Sr[LiAl_3N_4]:Eu^{2+}$ (SLA),[7] $Sr[Mg_3SiN_4]:Eu^{2+}$ (SMS),[8] or $Sr[Li_2Al_2O_2N_2]:Eu^{2+}$ (SALON).[9] Even though SMS exhibits an emission maximum in the desired spectral region at $\lambda_{max} = 615$ nm and a very narrow emission band with a full width at half-maximum (fwhm) of 43 nm/1170 cm^{-1}, high thermal quenching prevents its application in pc-LEDs. SLA ($\lambda_{max} = 654$ nm, fwhm = 50 nm/1180 cm^{-1}) and the recently reported SALON ($\lambda_{max} = 614$ nm, fwhm = 48 nm/1286 cm^{-1}) show better thermal performance, but emission band widths of both

[a] E. Elzer, Prof. Dr. W. Schnick
Department of Chemistry
University of Munich (LMU)
Butenandtstrasse 5–13, (D) 81377 Munich (Germany)
E-mail: wolfgang.schnick@uni-muenchen.de
Homepage: https://www.cup.uni-muenchen.de/ac/schnick/
[b] Dr. P. Strobel, V. Weiler, Dr. P. J. Schmidt
Lumileds Phosphor Center Aachen
Philipsstrasse 8, 52068 Aachen (Germany)
[c] M. R. Amin, Prof. Dr. A. Moewes
Department of Physics and Engineering Physics
University of Saskatchewan
116 Science Place, Saskatoon, Saskatchewan, S7N 5E2 (Canada)

Supporting information for this article is available on the WWW under https://doi.org/10.1002/chem.202104121

compounds do not yet match the target value of 30 nm, proposed for a high-performance red phosphor.[1]

In the pursuit of Eu^{2+} doped host lattices with an even narrower emission band, the incorporation of Be^{2+} into the anionic networks of nitrides may evolve as a viable solution also for narrow-red emitting materials. Compared to Al^{3+} or Si^{4+}, Be^{2+} has a lower formal charge, which can lead to host lattices with a large κ, as already demonstrated with the discovery of the cyan-emitting oxonitridoberyllate $Sr[Be_6ON_4]:Eu^{2+}$,[10] the blue-emitting oxoberyllates $AELi_2[Be_4O_6]:Eu^{2+}$ (AE = Sr, Ba),[11] the blue-emitting nitridoberyllates $MBe_{20}N_{14}:Eu^{2+}$ (M = Sr, Ba),[12] or the red-emitting nitridoberylloaluminate $Sr_2[BeAl_3N_5]:Eu^{2+}$.[13]

As already mentioned, the 5d energy levels are highly sensitive towards the local environment of the activator ion. This enables tuning of the shape and position of the emission band by tailoring the local structure around the activator. With respect to a free Eu^{2+} ion, the energy of the lowest excited state of Eu^{2+} ions in a host lattice is affected by the nephelauxetic effect and the crystal field splitting. Usually, a covalent activator-ligand bond and a strong crystal field result in a significant lowering of the energetic position of the 5d orbitals. Therefore, the distance between the ground state and the excited state is reduced, resulting in a red-shifted emission. The crystal field splitting depends on the local environment, especially the activator-ligand bond length, the coordination number and the shape of the coordination polyhedron around the activator. Thus, the size of the cations substituted by Eu^{2+} can be used to modify the emission color of a phosphor. If smaller cations (for example, Sr^{2+}) are replaced by larger ones (for example, Ba^{2+}), the metal-ligand distances and the volume of the coordination polyhedra usually increase, leading to a weaker crystal field splitting, shifting the emission bands towards the blue spectral region. The opposite case is seen in $M[Mg_3SiN_4]:Eu^{2+}$ (M = Sr, Ba),[8,14] and $M[Mg_2Al_2N_4]:Eu^{2+}$ (M = Ca, Sr, Ba),[15] where a trend to red-shifted emission in the sequence Ca < Sr < Ba has been observed. The emission of both phosphors with M = Ba is discussed to originate from two emission processes: regular $4f^5d^1 \rightarrow 4f^7$ Eu^{2+} emission accompanied by trapped exciton emission, which is characterized by a large Stokes shift, a broad emission band and unusual temperature behavior.[14,15] Trapped-exciton emission has also been observed in nitridoberyllate phosphors, such as $SrBeSi_2N_4:Eu^{2+}$ and $MBe_{20}N_{14}:Eu^{2+}$ (M = Sr, Ba).[12,16] The compounds exhibiting such anomalous luminescence show unexpected behavior at low temperatures: The emission maximum is shifted to longer wavelengths at lower temperatures compared to the values obtained at room temperature.[14,15,17]

In the pursuit of the discovery of new phosphors with optimized luminescence properties different strategies have been proposed, for example mineral prototype evolution strategy, single-particle diagnosis approach, machine learning or cation substitution strategy.[18] The relation of Eu^{2+} luminescence and the crystal structure of the host lattice motivates substitution in already known structures as well as exploration of completely new structures to contribute to the understanding of structure-property relationships.

In this contribution, we report on optical luminescence of $Ba_2[BeAl_3N_5]:Eu^{2+}$ and the solid solution series $Sr_{2-x}Ba_x[BeAl_3N_5]:Eu^{2+}$ (x = 0.5, 1.0, 1.5), as well as their syntheses and electronic properties. Upon irradiation with blue light, the nitridoberylloaluminates exhibit intense orange to red luminescence. In contrast to the usual trend, the emission maximum in the nitridoberylloaluminates $Sr_{2-x}Ba_x[BeAl_3N_5]:Eu^{2+}$ ($x > 0$) is inversely shifted to higher wavelengths by the incorporation of the larger cation Ba^{2+}. This contribution shows that even small changes in the local environment in the investigated nitridoberylloaluminates have a significant effect on the luminescence, since activator concentration and anomalous emission can be ruled out as causes for the unexpected, red-shifted emission with increasing size of the alkaline earth element.

Results and Discussion

Synthesis and chemical analysis

A modification of the reported synthesis for $Sr_2[BeAl_3N_5]:Eu^{2+}$,[13] gave access to a solid solution series with the nominal composition $Sr_{2-x}Ba_x[BeAl_3N_5]:Eu^{2+}$ (x = 0.5, 1.0 and 1.5) and $Ba_2[BeAl_3N_5]:Eu^{2+}$. The products were obtained as crystalline powders with orange body color and red luminescence upon irradiation with blue light. The morphology of the crystals is shown in Figure S2. The atomic ratio of Sr : Ba : Al : N (Table 1), as obtained from EDX measurements, range within the estimated standard deviations from the intended sum formulas for the solid solution series $Sr_{2-x}Ba_x[BeAl_3N_5]:Eu^{2+}$.

Beryllium usually cannot be detected with this method. The oxygen content is insignificant within the estimated standard deviations and was only detected for the Sr-rich representatives of the solid solution series (x = 0.5, 1.0). A possible reason might be the hydrolysis sensitivity of the investigated powder samples. As already mentioned in the experimental section the formation of MBe_2N_2 (M = Sr, Ba) and SrO as impurity phases hampered the preparation of a defined composition with regard to the atomic ratio of Sr : Ba for the solid solution phases.

Crystal structure

Based on the crystal structure solution and refinement (SHELX-2014),[19] $Ba_2[BeAl_3N_5]:Eu^{2+}$ crystallizes in space group $P\bar{1}$ (no. 2)

Table 1. EDX results of $Sr_{2-x}Ba_x[BeAl_3N_5]:Eu^{2+}$ (x = 0, 0.5, 1.0, 1.5, 2.0). Theoretical values (th.) and experimental values (exp.) in mol% for each composition with standard deviations in parentheses.

	$Sr_{2-x}Ba_x[BeAl_3N_5]:Eu^{2+}$									
x	0		0.5		1.0		1.5		2.0	
	th.	exp.	th.	exp.	th.	exp.	th.	exp.	th.	exp.
Sr	20	25(3)	15	11(3)	10	9(1)	5	5(1)	0	0
Ba	0	0	5	7(2)	10	12(2)	15	14(1)	20	16(3)
Al	30	30(4)	30	32(4)	30	34(3)	30	33(2)	30	36(2)
N	50	45(6)	50	43(4)	50	44(3)	50	48(3)	50	49(3)
O	0	0	0	7(7)	0	1(1)	0	0	0	0

isotypical to $Sr_2[BeAl_3N_5]:Eu^{2+}$.[13] During the refinement of the crystal structure the small amount of Eu^{2+} was neglected, due to the insignificant contribution to the scattering density. Crystallographic data of the Ba-containing phase show an increase of the unit cell volume (~7%) compared to $Sr_2[BeAl_3N_5]:Eu^{2+}$, due to the incorporation of the larger Ba^{2+} ion (Table 2).

Detailed crystallographic data, atomic coordinates, Wyckoff positions, isotropic displacement parameters, anisotropic displacement parameters and selected distances and angles of $Ba_2[BeAl_3N_5]:Eu^{2+}$ are summarized in the Supporting Information (Tables S3–S7). Detailed information on the single-crystal data of $Ba_2[BeAl_3N_5]:Eu^{2+}$ are provided free of charge by the joint Cambridge Crystallographic Data Centre and Fachinformationszentrum Karlsruhe Access Structures service. Deposition Number CSD-2121521 (for $Ba_2[BeAl_3N_5]:Eu^{2+}$) contains the supplementary crystallographic data for this paper.

The crystal structure of $Ba_2[BeAl_3N_5]:Eu^{2+}$ (Figure 1a) consists of edge- and vertex-sharing AlN_4 tetrahedra and trigonal-planar BeN_3 units. Each AlN_4 tetrahedron shares one edge with another AlN_4 tetrahedron building a bow-tie unit ($[Al_2N_6]^{12-}$) and each BeN_3 unit is connected to a second BeN_3 unit over a common edge, building a planar $[Be_2N_4]^{8-}$ unit (Figure 1b). These building units are further connected by common vertices forming a three-dimensional anionic network, which contains channels filled with Ba^{2+} (and Eu^{2+}, when doped) for charge neutrality. The alkaline earth (*AE*) ions are distributed over three different coordination sites (Ba1, Ba2 and Ba3) and coordinated by seven (Ba1) and eight (Ba2 and Ba3) N atoms, respectively (Figure 1c).

The interatomic distances between Ba atoms and N atoms are in the range of 2.719(5)–3.243(4) Å, which is comparable with other Ba-containing nitrides with a coordination number (CN) of eight (Figure S3). The increase of the distances in the sequence $d_{Ba1-N} < d_{Ba2-N} < d_{Ba3-N}$ corresponds well with the higher CN around Ba2 and Ba3. Both effects explain the increased thermal displacements of the Ba2/Ba3 sites in comparison to Ba1 (Table S5). The different distances are also reflected in the polyhedral volumes, which are significantly smaller around Ba1 (31.64 Å^3) relative to Ba2 (46.15 Å^3) and Ba3 (44.41 Å^3).

The bulk phase composition of the samples was determined by Rietveld refinement of powder X-ray diffraction data (Table S8). For the refinement of $Sr_{2-x}Ba_x[BeAl_3N_5]:Eu^{2+}$ ($x > 0$), the structural model of $Ba_2[BeAl_3N_5]:Eu^{2+}$ from single-crystal X-ray diffraction data was used. Representative for all samples, the plot of the Rietveld refinement of $Ba_2[BeAl_3N_5]:Eu^{2+}$ is shown in Figure 2, confirming $Ba_2[BeAl_3N_5]:Eu^{2+}$ as the main phase.

The sample contains small amounts of AlN and $BaBe_2N_2$ as impurity phases. Rietveld refinement plots for $Sr_{2-x}Ba_x[BeAl_3N_5]:Eu^{2+}$ ($x > 0$) are provided in the Supporting Information (Figure S4).

Due to the larger ionic radius of Ba^{2+} compared to Sr^{2+}, the lattice parameters of the samples are increasing with Ba^{2+} partially or completely occupying the Sr sites. Comparing the lattice parameters (Figure 3), an almost linear dependence on the atomic ratio Ba : Sr is observed.

As already discussed above, the structure provides three crystallographically independent AE^{2+} (AE^{2+} = Sr, Ba) sites (Figure 1c) with coordination polyhedra of different sizes and shapes. Since the local coordination around the cation replaced by Eu^{2+} can have a strong influence on the photoluminescence properties of the nitridoberylloaluminates, the occupation of Sr/Ba1, Sr/Ba2 and Sr/Ba3 sites was investigated using Rietveld refinements. A graphical representation of the site occupation

Table 2. Crystallographic data of $Ba_2[BeAl_3N_5]:Eu^{2+}$ compared to reported values for $Sr_2[BeAl_3N_5]:Eu^{2+}$.[13] Standard deviations in parentheses.

	$Sr_2[BeAl_3N_5]:Eu^{2+}$	$Ba_2[BeAl_3N_5]:Eu^{2+}$
Formula mass /g mol^{-1}	335.24	434.68
Crystal system	triclinic	
Space group	$P\bar{1}$ (no. 2)	
Formula units/cell	2	
Cell parameter /Å, °	$a = 6.061(2)$	$a = 6.1869(10)$
	$b = 6.982(3)$	$b = 7.1736(13)$
	$c = 7.872(4)$	$c = 8.0391(14)$
	$\alpha = 102.22(3)$	$\alpha = 102.754(8)$
	$\beta = 112.62(2)$	$\beta = 112.032(6)$
	$\gamma = 104.02(2)$	$\gamma = 104.765(7)$
Volume/Å^3	280.5(2)	299.24(9)
X-ray density/g cm^{-3}	3.969	4.824

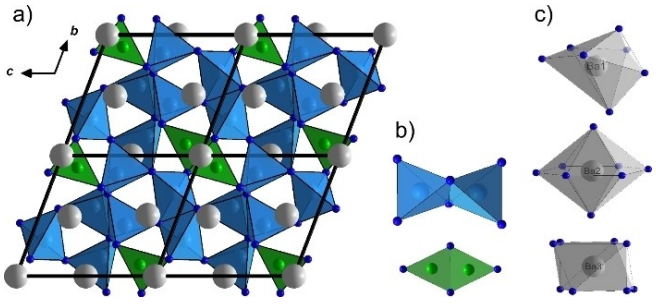

Figure 1. Crystal structure representation of $Ba_2[BeAl_3N_5]:Eu^{2+}$ with Al atoms (light blue), Be atoms (green),N atoms (blue) and Ba atoms (gray). a) view of 2×2×2-unit cells along [100]; b) bow-tie unit $[Al_2N_6]^{12-}$ (top, light blue) and $[Be_2N_4]^{8-}$ unit (bottom, green); c) coordination polyhedra (gray) around Ba1 (top), Ba2 (middle) and Ba3 (bottom).

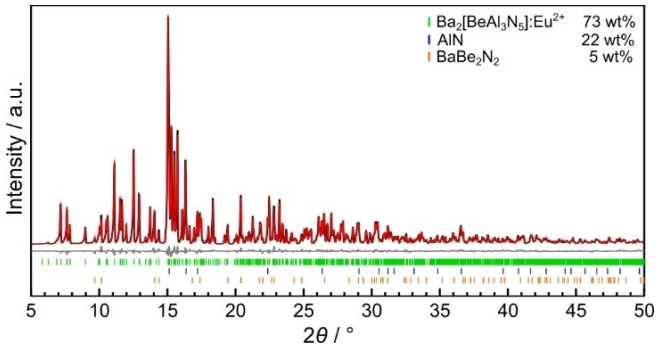

Figure 2. Rietveld refinement of $Ba_2[BeAl_3N_5]:Eu^{2+}$ (Mo $K_{\alpha 1} = 0.71073$ Å). Experimental data (black line), calculated pattern (red line) and difference curve (gray line). Tick marks: position of Bragg reflections of $Ba_2[BeAl_3N_5]:Eu^{2+}$ (green), AlN (blue), and $BaBe_2N_2$ (orange).

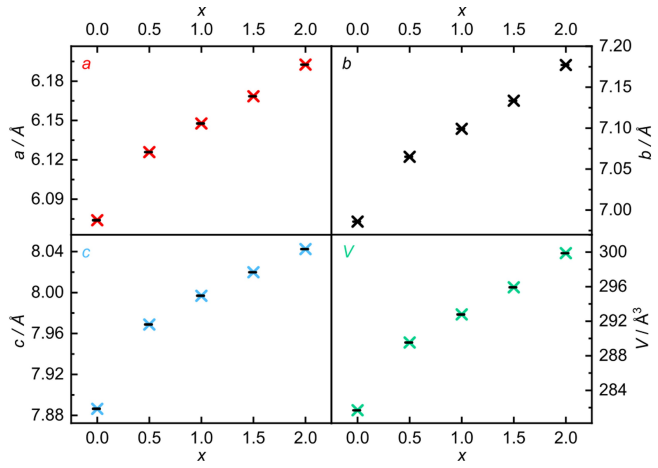

Figure 3. Comparison of the lattice parameters *a* (red), *b* (black), and *c* (light blue), and the volume of the unit cell *V* (green) of $Sr_{2-x}Ba_x[BeAl_3N_5]:Eu^{2+}$ with $x = 0$, 0.5, 1.0, 1.5 and 2.0 obtained from Rietveld refinements.

factors is illustrated in Figure 4, indicating a mixed occupancy of all three sites.

The refinement was restrained to allow only electroneutral sum formula. Therefore, the three crystallographic sites were assumed to be fully occupied while the Sr:Ba ratio was refined. According to the refinements, the atomic ratios of Sr:Ba are 1.3:0.7 ($x = 0.5$), 1.1:0.9 ($x = 1.0$) and 0.7:1.3 ($x = 1.5$).

Due to the different ionic radii of Ba^{2+} (1.42 Å, CN = 8) and Sr^{2+} (1.26 Å, CN = 8),[20] an ordering of the heavy atoms is plausible. The members of the solid solution, however, do not show ordering of the AE^{2+} ions, but indicate a mixed occupancy of all three sites (Figure 4). But the distribution of the larger Ba^{2+} ion is uneven across the possible sites. Ba^{2+} ions prefer the occupation of Sr/Ba2 and Sr/Ba3, probably based on the larger polyhedral volumes compared to the Sr/Ba1 site. The impact of these results will be further discussed in the luminescence section.

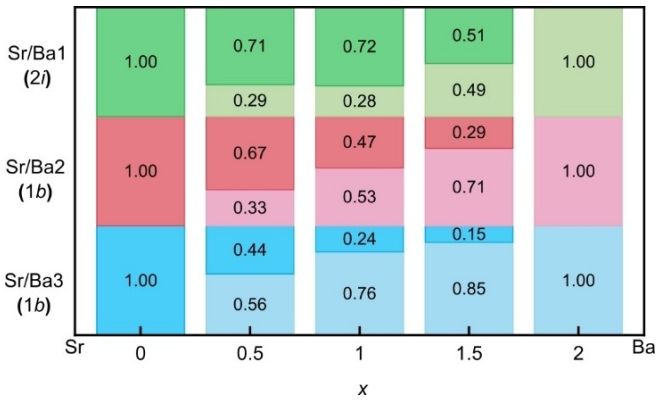

Figure 4. Graphical representation of the site occupation factors of the three crystallographic sites occupied by Sr and/or Ba in the solid solution series $Sr_{2-x}Ba_x[BeAl_3N_5]:Eu^{2+}$. Wyckoff positions of the respective sites are given in brackets. The darker color represents Sr, while the lighter color stands for Ba.

Electronic properties

The electronic properties of $M_2[BeAl_3N_5]:Eu^{2+}$ (M = Sr, Ba) were investigated by a combination of synchrotron-based soft X-ray absorption spectroscopy (XAS) and X-ray emission spectroscopy (XES), as well as DFT calculations. As the results for both compounds are quite similar, the XES, XAS, resonant inelastic X-ray scattering spectra (RIXS) and a non-resonant X-ray emission spectrum (NXES) for $Sr_2[BeAl_3N_5]:Eu^{2+}$ are shown in Figure 5, while the spectra for $Ba_2[BeAl_3N_5]:Eu^{2+}$ can be found in the Supporting Information (Figure S5). The solid black line shown in Figure 5b corresponds to the experimental PFY for $Sr_2[BeAl_3N_5]:Eu^{2+}$, which is compared to core hole (solid orange line) and ground state (dash-dotted orange line) calculations.

It is found that the experimental XAS spectrum is in good agreement with the core hole calculations, as all major features are reproduced at the correct energy positions and approximately at the correct peak heights. The comparison of the two calculated absorption spectra (Figure 5b, orange) to the measured spectrum (Figure 5b, black) makes it clear that the core hole concentration in the experiment lies somewhere between the two calculated cases. Therefore, the core hole concentration should be more dilute than the case we calculated, and which reflects 1 of 20 atoms in the supercell missing a 1s electron. A more diluted core hole concentration (and hence larger supercell) was computationally not feasible due to the increased cpu time that would be required.

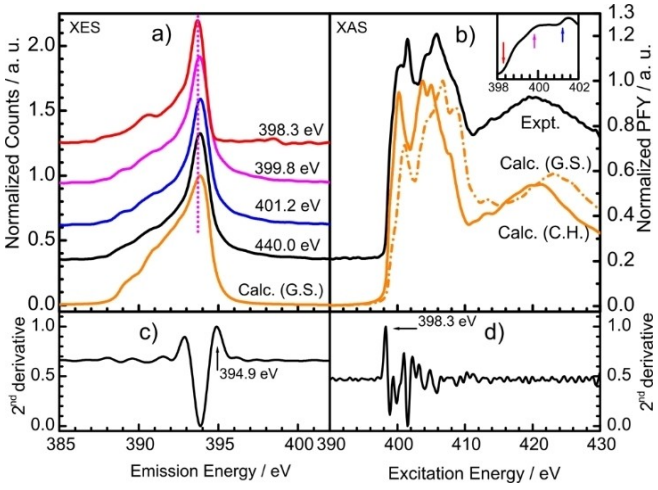

Figure 5. Experimental and calculated N K-edge XES and XAS spectra of $Sr_2[BeAl_3N_5]:Eu^{2+}$. a) NXES spectrum (black) excited at 440.0 eV and RIXS spectra (red, magenta, and blue) collected at 398.3 eV, 399.8 eV, and 401.2 eV are compared with ground state calculations (orange). The vertical dotted magenta line indicates that the highest emission energy is observed at the highest excitation energy in the RIXS spectra, which indicates an indirect band gap; b) Comparison of experimental PFY (black), core hole (C.H.) and ground state (G.S.) calculations of N K-edge XAS spectra. The small color coded arrows in the embedded figure indicate where in the conduction band (CB) the N 1s electron was excited to obtain the emission spectra of the corresponding color; c) Second derivative of the NXES spectrum, with peaks that are above the noise level and are corresponding to the valence band edge indicated by the arrow; d) Second derivative of PFY of XAS spectrum with peaks corresponding to CB edge indicated by the arrow.

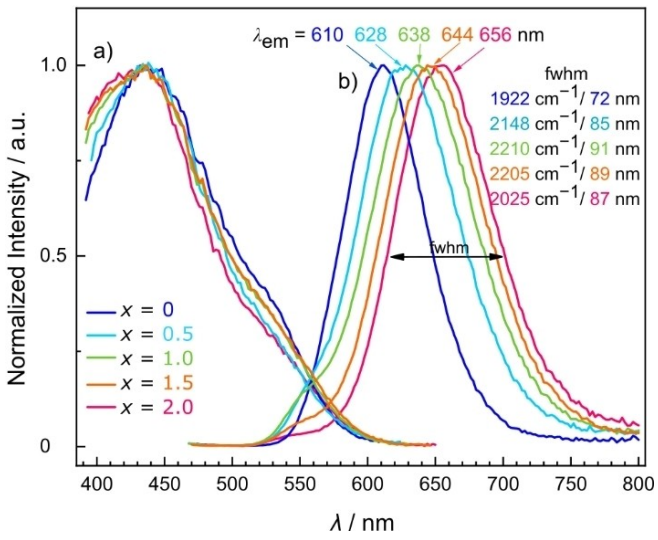

Figure 6. Normalized photoluminescence spectra of single particles of $Sr_{2-x}Ba_x[BeAl_3N_5]:Eu^{2+}$ with $x=0$ (dark blue), 0.5 (light blue), 1.0 (green), 1.5 (orange), 2.0 (pink)). a) Excitation spectra ($\lambda_{obs}=626$–670 nm), b) Emission spectra ($\lambda_{exc}=440$–450 nm).

As the absorption and emission spectra are proportional to the unoccupied and occupied pDOS, respectively their separation can be used to determine the electronic band gap, using the second derivative method. Here, the valence band (VB) and the conduction band (CB) edges are taken to be the first peaks in the second derivative above the noise at the upper edge of the NXES and lower edge of the XAS spectra, respectively, as indicated by the arrows in Figure 5c+d. From the band edges (Figure 5 and Figure S5) the estimated band gap is found to be 3.4 ± 0.3 eV for $Sr_2[BeAl_3N_5]:Eu^{2+}$ and 3.1 ± 0.3 eV for $Ba_2[BeAl_3N_5]:Eu^{2+}$, respectively. This result must be adjusted to account for the effect of the N 1s core hole that is created during the excitation process. Applying a DFT-derived correction of 0.1 eV the final experimental band gaps are found to be 3.5 ± 0.3 eV ($M=$Sr) and 3.2 ± 0.3 eV ($M=$Ba), respectively. The calculated band gap using PBE-GGA is found to be 2.8 eV ($M=$Sr) and 2.56 eV ($M=$Ba), respectively. This underestimation is typical for DFT and can be improved by using the modified Becke-Johnson (mBJ) exchange-correlation potential.[21] In this case, the calculated band gaps are found to be 4.2 eV ($M=$Sr) and 3.6 eV ($M=$Ba). A summary of the band gap values can be found in Table 3.

The band structure of $M_2[BeAl_3N_5]:Eu^{2+}$ ($M=$Sr, Ba) was calculated using the mBJ exchange-correlation potentials (Figure S6). The calculations indicate an indirect band gap for both materials with the valence band (VB) maximum at the T point for both compounds and the conduction band (CB) minimum at the Γ point for $Sr_2[BeAl_3N_5]:Eu^{2+}$ and Z point for $Ba_2[BeAl_3N_5]:Eu^{2+}$, respectively. The pDOS of both compounds (Figure S7) show high similarity with other materials based on XN_4 ($X=$Li, Al, Mg, Si) tetrahedra, for example, SLA,[22] $Li_2Ca_2[Mg_2Si_2N_6]:Eu^{2+}$,[23] or $Ba[Li_2[Al_2Si_2]N_6]:Eu^{2+}$,[23] where the upper VB is dominated by N p states and the lower VB is characterized by X s/p states. Meanwhile, the alkaline earth ion d states strongly contribute to the lower CB. Based on the definition of Dorenbos, there are two types of compounds: type I compounds, where the bottom of the CB is dominated by alkaline earth ions which are replaced by rare earth ions, and type II compounds, where the lower CB is dominated by ions that are not replaced by the rare earth ion.[24] Typically, type I compounds show an increasing band gap with smaller size of the alkaline earth, which is in accordance with the values obtained for $M_2[BeAl_3N_5]:Eu^{2+}$ ($M=$Sr, Ba), where Sr-containing phosphor show larger band gap values (Table 3).

Table 3. Determined band gap (Δ) values for $M_2[BeAl_3N_5]:Eu^{2+}$ ($M=$Sr, Ba) in eV obtained from X-ray spectroscopy (XES/XAS), DFT-calculations (GGA/mBJ) and UV-Vis spectroscopy (Tauc, direct and indirect).

M	$\Delta_{XES/XAS}$	Δ_{GGA}	Δ_{mBJ}	$\Delta_{Tauc,\ direct}$	$\Delta_{Tauc,\ indirect}$
Sr	3.5 ± 0.3	2.8	4.2	3.8[13]	3.1
Ba	3.2 ± 0.3	2.6	3.6	3.5	3.0

UV-vis spectroscopy

Additionally, the optical band gaps of $Sr_2[BeAl_3N_5]:Eu^{2+}$ and $Ba_2[BeAl_3N_5]:Eu^{2+}$ were estimated from reflectance data and compared to the ones obtained from XAS/XES experiments and DFT calculations. The reflectance spectra R were converted to pseudoabsorption spectra using the Kubelka-Munk function $F(R)=(1-R)^2/(2R)$ (Figure S8).[25] The optical band gaps were determined through a linear fit of the data at the infliction point from the Tauc plots $([F(R)\ h\nu]^{1/n}$ with $n=1/2$ for a direct and $n=2$ for an indirect allowed transition for a better comparison with the literature (direct band gap for $Sr_2[BeAl_3N_5]:Eu^{2+}$ of 3.8 eV).[13] The values are summarized in Table 3 and are approximately in the same range, as the calculated (GGA and mBJ) and experimentally (XES/XAS) determined band gaps.

Luminescence

Luminescence measurements were carried out on samples with various compositions. Excitation and emission spectra of single particles of the solid solution series $Sr_{2-x}Ba_x[BeAl_3N_5]:Eu^{2+}$ ($x=$ 0–2.0) are displayed in Figure 6 (2 mol% Eu^{2+} concentration referred to Sr/Ba).

The excitation spectra in Figure 6a show that all members of the solid solution series can be excited with blue light with a maximum absorption around 440 nm. Compared to the Sr-containing nitridoberylloaluminate, $Ba_2[BeAl_3N_5]:Eu^{2+}$ exhibits a red-shifted emission maximum at $\lambda_{em}=656$ nm with a fwhm of $\approx$87 nm/2025 cm^{-1}. The position of the emission maximum and the shape of the emission band obtained from single particles are comparable to those obtained from bulk samples (Supporting Information, Figure S10). Therefore, the luminescence properties of the bulk samples can be assigned to $Ba_2[BeAl_3N_5]:Eu^{2+}$ and rules out a possible contribution to the red emission by the side phase $BaBe_2N_2$. The value of the

internal quantum efficiency (IQE) at room temperature for $Ba_2[BeAl_3N_5]:Eu^{2+}$ is 44%, which is similar to $Sr_2[BeAl_3N_5]:Eu^{2+}$ (33%).[13] Overall, the photoluminescence properties for $Ba_2[BeAl_3N_5]:Eu^{2+}$ are comparable to other nitrides, some of which are summarized in Table 4.

To investigate the effect of the substitution of Sr^{2+} with Ba^{2+} on the Eu^{2+} luminescence in $Sr_{2-x}Ba_x[BeAl_3N_5]:Eu^{2+}$, luminescence emission spectra of samples with $x=0$, 0.5, 1.0, 1.5 and 2.0 were measured (Figure 6b). The emission maxima obtained from samples of the solid solution series show tunable emission between 610 to 656 nm through the compositional variable x (Figure 7).

The fwhm values for $x=0$ (72 nm/1922 cm^{-1}) and $x=2$ (87 nm/2025 cm^{-1}) are slightly smaller with values around 2000 cm^{-1}, while in $Sr_{2-x}Ba_x[BeAl_3N_5]:Eu^{2+}$ with $x=0.5$, 1.0 and 1.5 the fwhm is increased up to 2200 cm^{-1}. The fwhm broadening is caused by varying Eu–N distances, resulting from mixed occupation of the three alkaline earth sites as discussed in the crystal structure section. Furthermore, in the samples with mixed occupation of the Sr/Ba sites, a second emission maximum occurs at shorter wavelengths, peaking around 550 nm. The intensity of this second emission maximum is very weak and almost identical for the samples with $x=0.5$ and 1.0 and decreases even further in the sample with $x=1.5$. Comparing the low-temperature measurements of $Sr_2[BeAl_3N_5]:Eu^{2+}$[13] and $Ba_2[BeAl_3N_5]:Eu^{2+}$ (Figure S10) only one broad emission band is observed for the Ba compound, while the superposition of three emission maxima is observed at 6 K for $Sr_2[BeAl_3N_5]:Eu^{2+}$. In the mixed phases, it can be observed that this second emission maximum also decreases in intensity as the Sr content of the compound decreases. Therefore, the assumption is that this emission maximum originates from Eu^{2+} on the Sr/Ba1 site which contains the highest Sr content according to the Rietveld refinement (Figure 4).

Table 4. Luminescence properties and coordination number (CN) of selected orange-red emitting Eu^{2+} doped (oxo)nitrides.

Compound	λ_{em} /nm	λ_{exc} /nm	Fwhm /nm	Fwhm /cm^{-1}	CN	Ref.
$Ba_2[BeAl_3N_5]$	656	440	87	2025	7, 8	
$Ca[Mg_2Al_2N_4]$	606	440	67	1815	8	[15]
$Sr[Mg_2Al_2N_4]$	612	440	82	1823	8	[15]
$Sr_2[BeAl_3N_5]$	612	440	71	1899	7, 8	[13]
$Sr[Li_2Al_2O_2N_2]$	614	460	48	1286	8	[9]
$Sr[Mg_3SiN_4]$	615	440	43	1170	8	[8]
$Sr_2[MgAl_5N_7]$	633	440	78	1940	8	[26]
$Sr[LiAl_3N_4]$	654	440	50	1180	8	[7]
$Ba[Mg_2Al_2N_4]$	666	440	104	2331	8	[15]
$Sr_4[LiAl_{11}N_{14}]$	670	460	85	1880	8	[27]

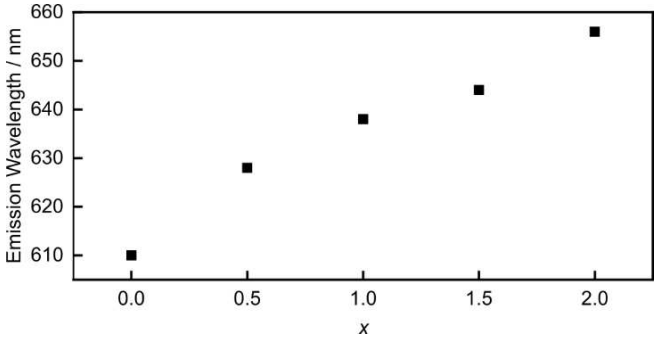

Figure 7. Correlation between the increasing Ba content with different x values and the emission wavelength from the luminescence measurements of bulk samples.

Cationic substitution is often used to alter the emission color of nitride phosphors, as the emission is strongly influenced by the local environment around the activator Eu^{2+}. Generally, the substitution of a smaller ion by a bigger one should lead to a smaller crystal field splitting and therefore shifting the emission color to shorter wavelengths.[3] Contrary to such observations, the emission of the solid solution series $Sr_{2-x}Ba_x[BeAl_3N_5]:Eu^{2+}$ is inversely shifted from 610 towards 656 nm with increasing Ba content as illustrated in Figure 7. The small leap in the position of the emission maximum observed between $x=0$ and $x=0.5$ is consistent with the interval observed analyzing the lattice parameter dependence on the Ba : Sr ratio, displayed in Figure 3.

Possible reasons for the uncommon, inverse-tunable red emission of $Sr_{2-x}Ba_x[BeAl_3N_5]:Eu^{2+}$ will be discussed in the following section. Such a red-shifted emission can be associated with the activator concentration, the occurrence of anomalous trapped exciton emission or occur due to a change in the local environment around Eu^{2+} without necessarily changing the crystal structure of the compound.[17a,28]

In crystal structures with multiple crystallographic sites for the incorporation of the activator, the activator can act as donor and acceptor, enabling energy transfer between the activator ions. Typically, the probability for an energy transfer depends on the distance between the Eu^{2+} atoms, therefore a red-shift of the emission with increasing activator concentration can take place, as already observed in different phosphors (for example, $M_2Si_5N_8:Eu^{2+}$ (M = Sr, Ba),[28a,29] or $Ca_{2-x}Eu_xSiO_4$[30]). Luminescence spectra of bulk samples of $Ba_2[BeAl_3N_5]:Eu^{2+}$ with a nominal Eu^{2+} concentrations of 0.3, 1, 2, 3, and 4 mol% referred to Ba are shown in the Supporting Information (Figure S9) and were compared with the reported spectra for $Sr_2[BeAl_3N_5]:Eu^{2+}$.[13]

In the literature, it has been reported that the location of the emission maximum does not change as the Eu content increases for $Sr_2[BeAl_3N_5]:Eu^{2+}$.[13] A comparable behavior was observed for $Ba_2[BeAl_3N_5]:Eu^{2+}$. Phase-pure samples will be necessary to further investigate luminescence properties in even more detail. Based on the current data, a red-shift of the emission due to increasing activator concentrations seems to be rather unlikely.

As anomalous trapped exciton emission is known to occur more likely in phosphors with Eu^{2+} on sites with high coordination number and large activator-ligand bond lengths,[28a] temperature-dependent emission measurements were performed to investigate the luminescence properties of the title compounds at lower temperatures (Figures S10–S12). The obtained spectra show no significant shift of the emission maxima at lower temperatures, suggesting that anomalous emission is an unlikely explanation for the unusual inverse shift of the emission maxima to higher wavelengths.

The third option to discuss is the dependence of the emission on structurally related properties, especially of Eu^{2+} states influenced by its surrounding ligands. As already stated in the introduction, the 4f–5d transition, which defines the excitation and emission properties of Eu^{2+} doped phosphors, is highly sensitive toward the local coordination environment around the activation ion. When Eu^{2+} replaces Sr^{2+} in $Sr_2[BeAl_3N_5]:Eu^{2+}$, no structural changes are expected, as the ionic radii of both ions are quite similar [Eu^{2+}: 1.25 Å (CN = 8) and 1.20 Å (CN = 7); Sr^{2+}: 1.26 Å (CN = 8) and 1.21 Å (CN = 7)].[20] The situation is quite different with Ba^{2+}, as the ionic radius is larger than that of Eu^{2+} [Ba^{2+}: 1.42 Å (CN = 8) and 1.38 Å (CN = 7)].[20] Therefore, incorporation of Eu^{2+} on a larger crystallographic site can lead to red-shifted emission due to local lattice rearrangement. Considering the stepwise substitution of the lighter alkaline earth ion by the heavier homologue in the solid solution series, the activator Eu^{2+} preferentially replaces Sr atoms due to the similar ionic radii. When the neighboring Sr atoms are gradually replaced by the larger Ba^{2+}, the strain of the Ba–N bond distances increases leading to shorter Sr–N and Eu–N bond lengths, in order to release lattice strain. The more Sr atoms are replaced by Ba^{2+}, the shorter the Eu–N (and Sr–N) distances become. Shorter activator-ligand distances increase the crystal field splitting of the 5d orbitals resulting in a continuous red-shifted emission, as discussed for example for $(Sr_{0.98-x}Ba_xEu_{0.02})Si_2O_2N_2$ ($x = 0$–0.63).[28b] Especially in crystal structures, where cations have a close proximity to each other, it is reasonable that the successive substitution of the smaller cations by a larger one can lead to local distortion and an increased lattice strain.[28b] As discussed in the crystal structure the anionic network of the nitridoberylloaluminates contains several channels which are filled with the alkaline-earth ions, therefore, replacing Sr^{2+} by Ba^{2+} would have a strong impact on several neighboring ions in this crystal structure. Therefore, it seems most likely, that the uncommon, inverse-tunable red emission of $Sr_{2-x}Ba_x[BeAl_3N_5]:Eu^{2+}$ is the result of a change in the local Eu^{2+} coordination, depending on the Sr : Ba ratio.

Conclusion

In this contribution we report on the synthesis of $Ba_2[BeAl_3N_5]:Eu^{2+}$ and the solid solution series $Sr_{2-x}Ba_x[BeAl_3N_5]:Eu^{2+}$ ($x = 0.5$, 1.0, 1.5) by high-temperature reaction in a hot isostatic press under 50 MPa N_2. The crystal structure of $Ba_2[BeAl_3N_5]:Eu^{2+}$ was solved and refined from a single-crystal, while the lattice parameters of the members of the solid solution series were determined by Rietveld refinement. The crystal structure is isotypic to the recently discovered nitridoberylloaluminate $Sr_2[BeAl_3N_5]:Eu^{2+}$ and consists of edge- and vertex-sharing AlN_4 tetrahedra and trigonal-planar BeN_3 units creating a highly condensed 3D network with three mixed occupied crystallographic Sr/Ba sites. $Ba_2[BeAl_3N_5]:Eu^{2+}$ shows an emission maximum at $\lambda_{em} = 656$ nm with a fwhm of ≈87 nm/2025 cm^{-1}, which is comparable to other narrow-band red-emitting phosphors like $M[Mg_2Al_2N_4]:Eu^{2+}$ (M = Sr, Ba), $MAlSiN_3$ (M = Ca, Sr),[31] α- and β-$Sr_2[MgAl_5N_7]:Eu^{2+}$, or $Sr_8[LiMg_2Al_{21}N_{28}]:Eu^{2+}$.[26] The Eu^{2+} emission can be continuously tuned from 610 to 656 nm by increasing the Ba content. Compared to narrow-band red-emitting phosphors like $Sr[LiAl_3N_4]:Eu^{2+}$, the members of the solid solution series show somewhat broader emission bands, most probably due to the convolution of the emission from three differently coordinated Eu^{2+} sites. In contrast to the usual trend, the emission maximum in the nitridoberylloaluminates $Sr_{2-x}Ba_x[BeAl_3N_5]:Eu^{2+}$ ($x = 0$–2) is inversely shifted to higher wavelengths by the incorporation of the larger cation Ba^{2+}. This fact emphasizes the importance of studies regarding the structures and properties of potential phosphors, since the Eu^{2+} emission can be significantly influenced by small local changes and distortions of the environment without necessarily changing the symmetry of the crystal.

In summary, the synthesis of the presented compounds and the study of their electronic and optical properties contributes to the elucidation of the so far little explored class of nitridoberylloaluminates and emphasizes their role in the discovery and development of new luminescent materials.

Acknowledgements

The authors thank Karl Adriaan Zijtveld (Lumileds Phosphor Center Aachen) for luminescence measurements, Dr. Christian Maak and Christian Minke for EDX measurements and Dr. Peter Mayer (all Department of Chemistry, University of Munich (LMU)) for collecting single-crystal X-ray diffraction data. The soft X-ray spectroscopy measurements were performed at the Canadian Light Source (CLS), which is funded by the Canada Foundation for Innovation, the Natural Science and Engineering Research Council of Canada (NSERC), the National Research Council Canada, the Canadian Institutes of Health Research, the Government of Saskatchewan, Western Economic Diversification Canada, and the University of Saskatchewan. The authors also acknowledge Compute Canada. The calculations presented in this paper were performed on the Cedar high-performance computing cluster, which is part of the WestGrid (www.westgrid.ca) and Compute Canada Calcul Canada (www.computecanada.ca). Open Access funding enabled and organized by Projekt DEAL.

Conflict of Interest

The authors declare no conflict of interest.

Data Availability Statement

The data that support the findings of this study are available in the supplementary material of this article.

Keywords: aluminium · beryllium · luminescence · nitrides · X-ray absorption spectroscopy

[1] M. Pattison, M. Hansen, N. Bardsley, C. Elliott, K. Lee, L. Pattison, J. Tsao, Office of Scientific and Technical Information (OSTI), **2020**.
[2] J. L. Leaño, M.-H. Fang, R.-S. Liu, *ECS J. Solid State Sci. Technol.* **2017**, *7*, R3111-R3133.
[3] L. Wang, R. J. Xie, T. Suehiro, T. Takeda, N. Hirosaki, *Chem. Rev.* **2018**, *118*, 1951–2009.
[4] A. Meijerink, G. Blasse, *J. Lumin.* **1989**, *43*, 283–289.
[5] R.-J. Xie, N. Hirosaki, T. Suehiro, F.-F. Xu, M. Mitomo, *Chem. Mater.* **2006**, *18*, 5578–5583.
[6] H. Watanabe, N. Kijima, *J. Alloys Compd.* **2009**, *475*, 434–439.
[7] P. Pust, V. Weiler, C. Hecht, A. Tucks, A. S. Wochnik, A. K. Henss, D. Wiechert, C. Scheu, P. J. Schmidt, W. Schnick, *Nat. Mater.* **2014**, *13*, 891–896.
[8] S. Schmiechen, H. Schneider, P. Wagatha, C. Hecht, P. J. Schmidt, W. Schnick, *Chem. Mater.* **2014**, *26*, 2712–2719.
[9] G. J. Hoerder, M. Seibald, D. Baumann, T. Schroder, S. Peschke, P. C. Schmid, T. Tyborski, P. Pust, I. Stoll, M. Bergler, C. Patzig, S. Reissaus, M. Krause, L. Berthold, T. Hoche, D. Johrendt, H. Huppertz, *Nat. Commun.* **2019**, *10*, 1–9.
[10] P. Strobel, T. de Boer, V. Weiler, P. J. Schmidt, A. Moewes, W. Schnick, *Chem. Mater.* **2018**, *30*, 3122–3130.
[11] P. Strobel, C. Maak, V. Weiler, P. J. Schmidt, W. Schnick, *Angew. Chem. Int. Ed.* **2018**, *57*, 8739–8743; *Angew. Chem.* **2018**, *130*, 8875–8879.
[12] E. Elzer, R. Niklaus, P. J. Strobel, V. Weiler, P. J. Schmidt, W. Schnick, *Chem. Mater.* **2019**, *31*, 3174–3182.
[13] E. Elzer, P. Strobel, V. Weiler, P. J. Schmidt, W. Schnick, *Chem. Mater.* **2020**, *32*, 6611–6617.
[14] S. Schmiechen, P. Strobel, C. Hecht, T. Reith, M. Siegert, P. J. Schmidt, P. Huppertz, D. Wiechert, W. Schnick, *Chem. Mater.* **2015**, *27*, 1780–1785.
[15] P. Pust, F. Hintze, C. Hecht, V. Weiler, A. Locher, D. Zitnanska, S. Harm, D. Wiechert, P. J. Schmidt, W. Schnick, *Chem. Mater.* **2014**, *26*, 6113–6119.
[16] P. Strobel, V. Weiler, P. J. Schmidt, W. Schnick, *Chem. Eur. J.* **2018**, *24*, 7243–7249.
[17] a) P. Dorenbos, *J. Phys. Condens. Matter* **2003**, *15*, 2645–2665; b) J. L. Sommerdijk, A. Bril, *J. Lumin.* **1976**, *11*, 363–367.
[18] a) M. Zhao, Q. Zhang, Z. Xia, *Acc. Mater. Res.* **2020**, *1*, 137–145; b) Y. Zhuo, A. Mansouri Tehrani, A. O. Oliynyk, A. C. Duke, J. Brgoch, *Nat. Commun.* **2018**, *9*, 1–10; c) N. Hirosaki, T. Takeda, S. Funahashi, R.-J. Xie, *Chem. Mater.* **2014**, *26*, 4280–4288; d) X. Zhou, J. Qiao, Z. Xia, *Chem. Mater.* **2021**, *33*, 1083–1098.
[19] G. M. Sheldrick, *Acta Crystallogr. Sect. C* **2015**, *71*, 3–8.
[20] R. D. Shannon, *Acta Crystallogr. Sect. A* **1976**, *32*, 751–767.
[21] F. Tran, P. Blaha, *Phys. Rev. Lett.* **2009**, *102*, 226401.
[22] T. M. Tolhurst, T. D. Boyko, P. Pust, N. W. Johnson, W. Schnick, A. Moewes, *Adv. Opt. Mater.* **2015**, *3*, 546–550.
[23] T. M. Tolhurst, P. Strobel, P. J. Schmidt, W. Schnick, A. Moewes, *J. Phys. Chem. C* **2017**, *121*, 14296–14301.
[24] P. Dorenbos, *J. Phys. Condens. Matter* **2005**, *17*, 8103–8111.
[25] a) R. López, R. Gómez, *J. Sol-Gel Sci. Technol.* **2012**, *61*, 1–7; b) J. Tauc, R. Grigorovici, A. Vancu, *Phys. Status Solidi B* **1966**, *15*, 627–637; c) P. Kubelka, *J. Opt. Soc. Am.* **1948**, *38*, 448–457.
[26] P. Wagatha, V. Weiler, P. J. Schmidt, W. Schnick, *Chem. Mater.* **2018**, *30*, 1755–1761.
[27] D. Wilhelm, D. Baumann, M. Seibald, K. Wurst, G. Heymann, H. Huppertz, *Chem. Mater.* **2017**, *29*, 1204–1209.
[28] a) Y. Q. Li, J. E. J. van Steen, J. W. H. van Krevel, G. Botty, A. C. A. Delsing, F. J. DiSalvo, G. de With, H. T. Hintzen, *J. Alloys Compd.* **2006**, *417*, 273–279; b) G. Li, C. C. Lin, W.-T. Chen, M. S. Molokeev, V. V. Atuchin, C.-Y. Chiang, W. Zhou, C.-W. Wang, W.-H. Li, H.-S. Sheu, T.-S. Chan, C. Ma, R.-S. Liu, *Chem. Mater.* **2014**, *26*, 2991–3001; c) J. L. Leano, Jr., C. O. M. Mariano, W. T. Huang, S. Mahlik, T. Lesniewski, M. Grinberg, H. S. Sheu, S. F. Hu, R. S. Liu, *ACS Appl. Mater. Interfaces* **2020**, *12*, 23165–23171; d) A. Lazarowska, S. Mahlik, M. Grinberg, C. C. Lin, R. S. Liu, *J. Chem. Phys.* **2015**, *143*, 134704.
[29] H. A. Höppe, H. Lutz, P. Morys, W. Schnick, A. Seilmeier, *J. Phys. Chem. Solids* **2000**, *61*, 2001–2006.
[30] Y. Sato, H. Kato, M. Kobayashi, T. Masaki, D. H. Yoon, M. Kakihana, *Angew. Chem. Int. Ed.* **2014**, *53*, 7756–7759; *Angew. Chem.* **2014**, *30*, 7890–7893.
[31] H. Watanabe, H. Wada, K. Seki, M. Itou, N. Kijima, *J. Electrochem. Soc.* **2008**, *155*, F31-F36.

Manuscript received: November 16, 2021
Accepted manuscript online: January 12, 2022
Version of record online: February 2, 2022